MARS
The International Journal of Mars Science and Exploration

MARS INFORMATICS
Open Access Journals

Science

Characterizing the sensitivity of daytime turbulent activity on Mars with the MRAMS LES: Early results

Lori K. Fenton[1] and Timothy I. Michaels[2]

[1]*Carl Sagan Center, SETI Institute; NASA Ames Research Center, MS 245-3, Moffett Field, CA 94035, USA, lfenton@carlsagancenter.org;* [2]*Southwest Research Institute, 1050 Walnut St., Suite 300, Boulder, CO 80302, USA*

Citation: Mars 5, 159-171, 2010; doi:10.1555/mars.2010.0007
History: Submitted: May 15, 2010; Reviewed: July 2, 2010; Revised: August 16, 2010; Accepted: August 27, 2010; Published: December 10, 2010
Editor: Robert M. Haberle, NASA AMES Research Center
Reviewers: Aymeric Spiga, Laboratoire de Météorologie Dynamique; Daniel Tyler, Jr., Oregon State University

Abstract

Background: Daytime convectively-driven boundary layer turbulence produces structures on scales smaller than a few kilometers that can only be resolved in modeling by large-eddy simulations (LES). These structures, when superimposed on larger-scale dynamically- and topographically-driven flows, describe the wind regime experienced by aeolian features on the surface of Mars. Because convective turbulence produces the small percentage of strong wind gusts that may exceed the saltation stress threshold, such activity must be considered in order to properly predict particle entrainment, particularly in an environment in which mean winds are generally much weaker than the saltation stress threshold. We present early results from large-eddy simulations that characterize the daytime turbulent wind distributions under varying local conditions.

Method: We have run several large-eddy simulations using the Mars Regional Atmospheric Modeling System (MRAMS) at two locations on Mars, the Viking Lander 1 and Phoenix landing sites. Most simulations were defined at L_s=120º, northern summer, but one set of simulations took place at L_s=300º, northern winter. We have tested a number of initial wind conditions, including cases with no mean wind, a weak wind that is uniform with height, wind speed shear that increases with height, and two cases of strong uniform winds with superimposed speed shear. The resulting friction velocity distributions have been fit to a two-parameter Weibull probability density function (PDF), providing parameters that could help to quantify the influence of convective turbulence on wind distributions.

Conclusion: Daytime convective turbulence considerably widens the distribution of friction velocities, increasing the probability that winds will exceed the stress threshold and mobilize sand grains on Mars. The amount of widening increases with insolation as determined by latitude, season, and local time. Although no initial wind is necessary to produce a high speed wind tail that exceeds the local saltation stress threshold, initial winds can add momentum to the model domain that can be mixed down to the surface further increasing the likelihood of strong near-surface winds. In most cases tested thus far, friction velocity fits to a two-parameter Weibull distribution produce shape parameter values ranging from 2.5 to 3, which are larger than those previously used, and scale parameter values approximately equal to the mean friction velocity. Preliminary estimates indicate that increasingly complex and realistic initial winds exhibit friction velocity distributions that depart significantly from the Weibull distribution, with shape parameter values that range up to ~7. Describing the PDF of LES friction velocities with a Weibull distribution has known inadequacies, represents to date the best available simple analytic description of wind distributions for the modeling community. Therefore, these fit parameters are best used with caution, especially in high wind events, and applied only to conditions similar to those modeled.

Introduction

A key goal of Mars science is to understand the present-day interaction between the atmospheric environment and the planet's surface that ultimately results in climatically- and geologically-important aeolian phenomena (*e.g.*, dust storms, dust devils, albedo changes, dune migration, and surface

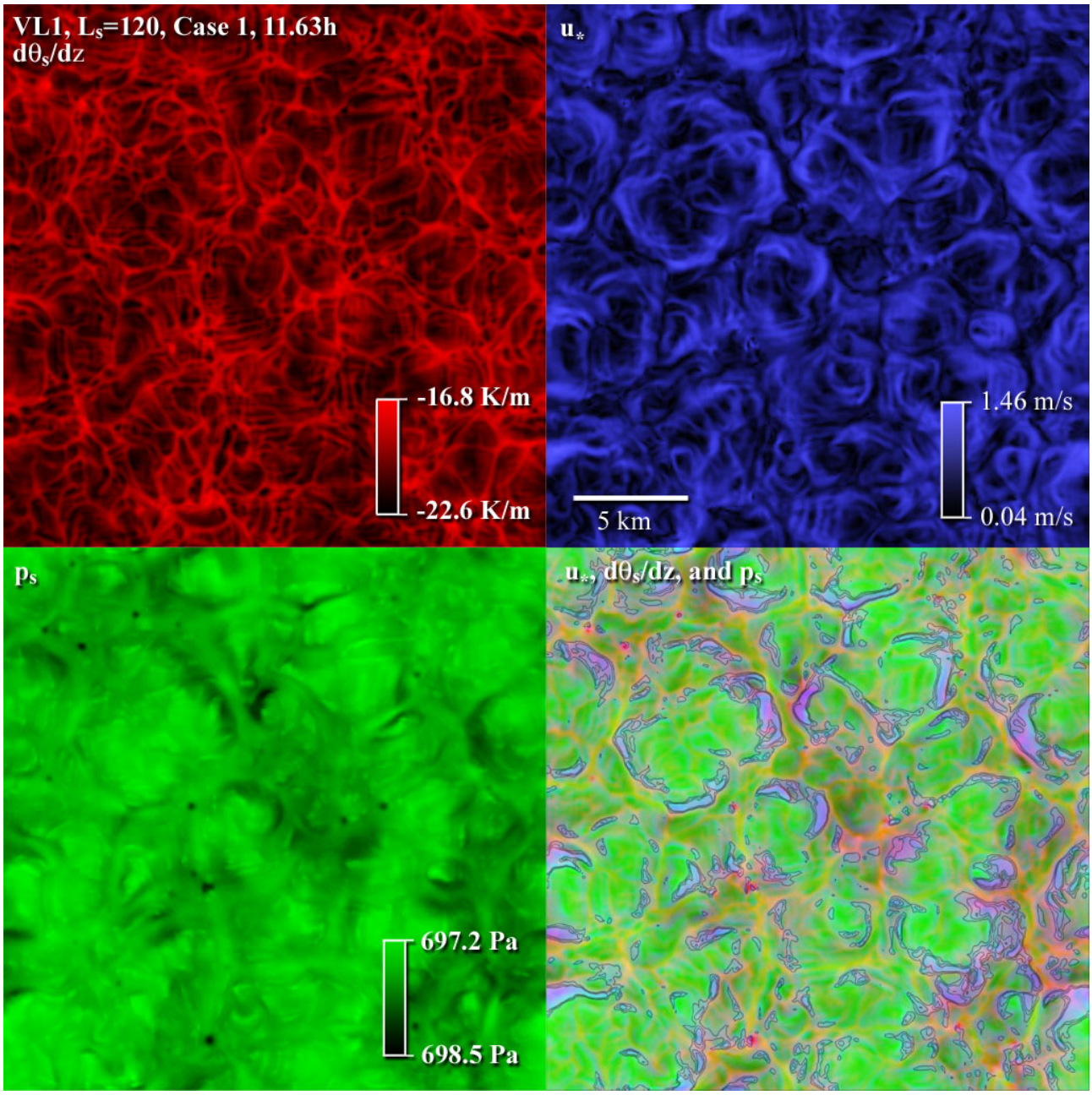

Figure 1. Horizontal near-surface slices through a LES domain, showing well-developed convection cells 2-6 km wide. Top left: static stability $\partial\theta_s/\partial z$, top right: friction velocity u_*, bottom left: air pressure p_s, bottom right: composite of the other three panels, including blue contours outlining the top 80%, 90%, and 95% friction velocities (figure1.jpg).

erosion). In order to fully understand any aeolian phenomenon, one important facet that must be characterized is the spatial and temporal structure of the near-surface wind. Such non-random wind structure may be conveniently classified (see next section for details) as either large-scale, mesoscale, or microscale. However, it must be remembered that in nature, the winds that any individual surface element interacts with are made of a complex and nonlinear integration of all three scales of wind structure. The work described here is a first step towards comprehensively characterizing the daytime turbulent winds (as a function of local time, latitude, and season) generated at the microscale on Mars, in part to enable the theoretical and numerical modeling of the planet's aeolian processes to progress to a new level of realism.

Background

The potential impact of *large-scale* atmospheric flows (*e.g.*, those resolved by a spatial grid interval of 100 km or more) on Mars surface-atmosphere interactions have been studied at length using global climate models (GCMs; *e.g.*, Haberle et al. 2003; Basu et al. 2004; Armstrong and Leovy 2005; Kahre et al. 2006). Even so, those studies could not directly incorporate the significant wind modulations that are due to

the direct and indirect effects of *mesoscale* topography and contrasts of soil thermophysical properties (*e.g.*, capable of being resolved using a spatial grid interval of 1-100 km), phenomena that are described by regional climate model studies (*e.g.*, Rafkin et al. 2001; Toigo et al. 2002; Rafkin and Michaels 2003; Spiga and Forget 2009). The most robust and consistent way to mitigate this particular problem is to run global climate simulations at the mesoscale. Such a practice is computationally quite difficult at the present time (*e.g.*, Spiga and Lewis (2010), this issue), leading to the possibility that computationally cheaper subgrid-scale parameterizations of these topographically-driven effects will be developed in the near future.

Boundary layer turbulence comprises a third realm, and results in significant local enhancements of larger-scale winds on which the turbulence is superposed (*e.g.*, Michaels 2002; Toigo et al. 2003; Michaels and Rafkin 2004; Tyler et al. 2008, Spiga et al., 2010), particularly during the daytime. Such turbulent structure occurs at the *microscale* (*e.g.*, resolvable using a grid interval on the order of 100 m or less), and are inherently three-dimensional. Large-eddy simulations (LES), which typically utilize horizontal grid intervals of 10-100 m in order to explicitly simulate the most energetic turbulent structures present in the near-surface atmosphere on Mars, are currently the dominant practical tool for characterizing atmospheric processes.

The vast majority of the aeolian-relevant microscale wind enhancements are due to turbulent wind gusts which generally share the direction of the spatial-mean wind – a characteristic that is consistent with the formation and evolution (via saltation, reputation, and creep of surface particles) of highly structured aeolian bedforms that have been observed on much of the martian surface. It should be noted that near-surface vertical vortices (including those that might be labeled dust devils) are particularly efficient at entraining any mobile surface dust into the atmosphere – however, by their very nature, such vortices do not contribute constructively to structured aeolian bedforms.

Figure 1 shows an example of the intricate pattern of near-surface turbulent activity typical of a convective boundary layer. This is a horizontal slice through a MRAMS large-eddy simulation (description in the Methods section) domain at z = 1.9 m near local noon at the Viking Lander 1 site (L_s = 120˚, no topography, no imposed mean wind, horizontal grid interval of 100 m). The top-left, top-right, and bottom-left panels show three different parameters, respectively: the near-surface static stability $\partial\theta_s/\partial z$ (in red); friction velocity u_* (in blue); and surface air pressure p_s (in green). The bottom-right panel shows a color composite of these three parameters, as well as contours outlining 80%, 90%, and 95% (by number) of the friction velocity values with the greatest magnitude. In the composite, convective cells ~2-6 km in width are outlined by narrow upwelling regions of relatively warm, buoyant air (where u_* is minimal, *i.e.*, in yellow). Within the cells, descending and compressing air produces broad regions of higher pressure (in green). After its descent, this air is heated by the hot surface (through infrared radiative transfer and to a lesser extent, molecular conduction) and makes its way towards the cell boundaries via a network of near-surface conduits (the thin yellow features within the larger-scale cells, also seen in red in the $\partial\theta_s/\partial z$ panel). As the air nears the narrow updrafts comprising the cell boundaries, it accelerates, producing strong wind gusts (contoured areas of high friction velocity). Strong vertical vortices, which can become visible as dust devils if they manage to lift dust from the surface, typically occur at the intersections of cells (where p_s is minimal, *i.e.*, magenta spots, also seen as dark spots in the p_s panel).

The importance of daytime microscale wind enhancements (exemplified in Figure 1) to surface-atmosphere interactions lies in the fact that the threshold friction velocities required to initiate sand saltation (and thus saltation-induced dust lifting) on Mars are roughly an order of magnitude larger than those on Earth (*e.g.*, Iversen and White 1982). As a result, the majority of winds on Mars may be too weak to initiate saltation, making particle entrainment more difficult relative to Earth (although it clearly does occur – *e.g.*, Sullivan et al. 2008). The minority wind populations that occupy the high-speed end of the wind magnitude probability distribution (*e.g.*, mesoscale fronts, microscale turbulent gusts, and strong vertical vortices) are thus most critical to particle entrainment on Mars. Due to this great emphasis on winds with relative low probability, any quantitative characterization of those winds must be based on a great number (greater than 10^4 over the local time interval of interest, based on our experience) of pertinent observations or model output values.

Unfortunately, the available Mars wind measurements are inadequate for this task. The Viking Landers recorded wind speed every 1 or 2 seconds for periods of tens of minutes (typically 500-1000 data points), although these sampling sessions were quite sporadic. Even allowing for co-adding of measurements from similar local times on different days, only datasets up to a few thousand points can be assembled. The Mars Pathfinder lander wind measurements have calibration issues (particularly during the daytime) and regardless, may have been too sporadic to assemble a large enough dataset to be relevant. The Phoenix lander provided the only other measurement of winds near the surface of Mars to date, but the accuracy and measurement cadence of those data are far below what is required for this work (Holstein-Rathlou et al., 2010).

Even in the absence of adequate observations, one can use theoretical and statistical considerations to qualitatively characterize the general form of the turbulent wind speed probability density function (PDF) as most closely matching a Weibull distribution (Tuller and Brett 1984). They found that terrestrial wind speeds approximate a Weibull distribution where the two orthogonal components of horizontal wind velocity follow a circular normal distribution, which was observed in hourly wind speeds where the effects of topography and frontal systems are minimized. Recently, the Weibull distribution has been shown to approximate three-hourly winds during the daytime, but not during the nighttime, in North America (He et al. 2010).

The two parameter form of the Weibull PDF:

$$PDF(u_*) = \left(\frac{k}{c}\right)\left(\frac{u_*}{c}\right)^{k-1} \exp\left[-\left(\frac{u_*}{c}\right)^{k}\right]. \quad (1)$$

in which u_* is friction velocity, k is the "shape parameter", and c is the "scale parameter" (see Figure 2). As its name suggests, the shape parameter controls the form of the distribution, ranging from exponential (k = 1), to Rayleigh (k = 2), to an approximation of a Gaussian (k = 3.6), to more skewed distributions at higher values of k. The scale parameter c describes how much the distribution is stretched the distribution is along the horizontal axis. When applied to turbulent wind speeds, an asymmetric high wind speed tail is present (containing the turbulent wind gusts) when values of the shape parameter are low (k < 3.6) and is enhanced when values of the scale parameter (c) increase. It is vitally important to note, however, that the Weibull distribution perfectly describes the wind speed PDF only in rare circumstances (Tuller and Brett 1984), and therefore should also not be expected to perfectly describe the *turbulent* wind speed PDF.

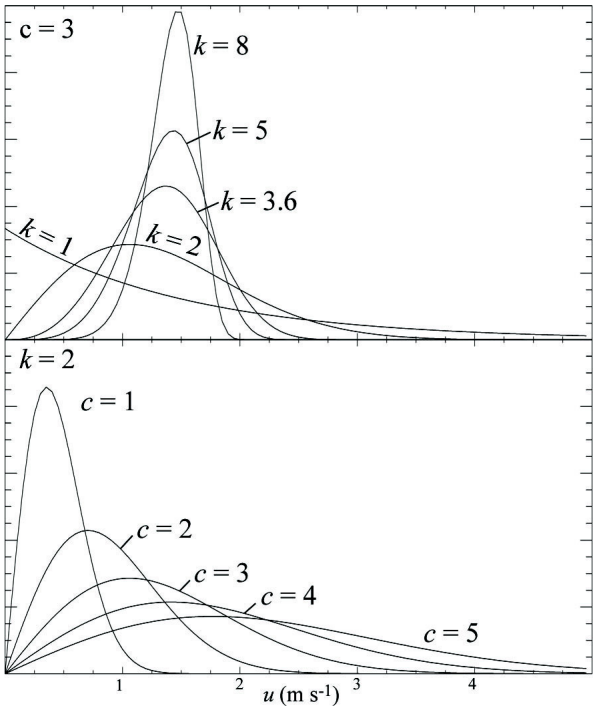

Figure 2. Examples of Weibull distributions for varying values of the shape parameter k and scale parameter c, following Eq. 1 (figure2.jpg).

Although the Weibull distribution is an often imperfect fit to turbulent wind speeds (and friction velocities), it is currently the most commonly used option for producing an analytical approximation for parameterizing wind gusts in atmospheric models. This approach is certainly more realistic than a strategy that has been used for decades in Mars climate modeling work to account for important subgrid-scale winds, in which the nominal saltation threshold is substantially reduced to grossly account for the unresolved higher-speed winds and wind gusts (*e.g.*, Toigo et al. 2002; Haberle et al. 2003). Indeed, there are currently more sophisticated (and realistic) methods in use that superimpose a Weibull distribution (or a set of them) on the mean friction velocities (*e.g.*, Newman et al. 2002; Basu et al. 2004; Michaels 2006; Michaels and Rafkin 2008).

The Weibull distributions employed by the global circulation modeling works of Newman et al. (2002) (k = 1.5) and Basu et al. (2004) (k = 1) for non-vortical subgrid-scale friction velocities (c = previous half-hourly output friction velocity at each surface grid cell) were based on fits to Viking Lander wind data made by Lorenz (1996). Michaels and Rafkin (2008) make an assumption that their explicit mesoscale modeling accounts for all important wind speed variability except for the subgrid-scale turbulent component, which is approximated with one of three Weibull distributions, depending on the local near-surface thermodynamic stability: a buoyantly unstable case (daytime case, with a pronounced high-speed tail; k = 1.2, c = current mesoscale friction velocity), a mechanically unstable case (moderate to small high-speed tail), and a stable scenario (little variance about the mean). It is important to note that to first order, the Weibull distribution that approximates a turbulent wind speed PDF is independent of whatever probability distribution(s) may describe other subgrid-scale spatial wind speed variability. Strictly speaking, one should therefore not use a Weibull distribution intended to approximate the turbulent wind speed PDF to approximate this other subgrid-scale variability (either explicitly or implicitly), and vice versa.

Estimates (measurement- or model-based) of the Weibull distribution parameters that approximate *turbulent* wind speed PDFs on Mars are not currently available in the literature. While superior to any other published estimates of wind distributions on Mars, Lorenz (1996) was limited to fitting Weibull distributions to wind speeds (rather than to friction velocities) averaged to a temporal resolution of 1/25 sol, and thus should be regarded most properly as estimates of the yearly non-turbulent wind speed PDFs at the Viking landing sites. This work aims to begin to provide estimates of the Weibull distribution parameters for the purely turbulent portion of the friction velocity PDF (during the daytime).

In order to make further progress in such model parameterizations and in the understanding of the nature of daytime turbulence on Mars, even with the lack of adequate observational data, large-eddy simulations may be employed. This modeling technique enables the generation of 40000 or more gridded and physically-consistent wind speed and friction velocity values per timestep (usually 1 s or less). There is no need for assumptions about the stationarity or homogeneity of the resolved turbulent structures (as is needed for a measured time series from a single surface station). Since it is a model, relevant parameter spaces may be explored at will, such as solar forcing (*e.g.*, due to latitude and the planet's rotation), surface pressure (*e.g.*, due to topography and seasonal cycles), and vertical wind shear. It

must be noted, however, that reality is so complex (and such models are so enabling) that the possible parameter space is gigantic – thus the work described here will only begin to explore the full breadth of plausibility.

Method

The Mars Regional Atmospheric Modeling System (MRAMS) is a non-hydrostatic, finite-difference, limited domain mesoscale model (Rafkin et al. 2001; Michaels 2002). It can perform LES when the subgrid-scale turbulence is modified to allow the explicit modeling of eddies down to very near the grid resolution, based on the method of (Deardorff 1980).

Table 1. Large-eddy simulations (table1.txt).

Location	Season (L_s)	Initial wind	Horizontal resolution
VL1	120º	Case 1	100 m
		Case 2	
		Case 3	
Phoenix	120º	Case 1	100 m
		Case 2	
		Case 3	
		Case 3, 10 m s^{-1}	
		Case 3, 20 m s^{-1}	
VL1	300º	Case 2	100 m
		Case 2	50 m

We have run several large-eddy simulations (see Table 1) at two locations on Mars: the approximate Viking Lander 1 (VL1) site (22.28˚ N, 312.05˚ E) and Phoenix Lander site (68.21˚ N, 234.26˚ E). Other than location and initial conditions (both inherited from mesoscale simulations and specified), each LES was run with the same general characteristics other than those listed in Table 2. In all cases but one the horizontal domain grid spacing was 100 m, spanning 24 km in each direction (240 × 240 grid points). The 99 vertical layers in this domain stretched in thickness from 4 m at the surface to 150 m near the top (at ~12 km). Full two-stream Mars-specific radiative transfer (with a static background dust opacity based on Mars Global Surveyor Thermal Emission Spectrometer observations) was used in these simulations. The dynamical time step was set to 1 s, and the radiative time step was 30 s.

Table 2. Characteristics of LES locations (table2.txt).

Location	Elevation (m)	Albedo	Thermal Inertia (J m^{-2} K^{-1} s$^{-0.5}$)	z_0 (m)
VL1	-3640	0.216	293.7	0.03
Phoenix	-4130	0.201	195.7	0.01

Most simulations were run at L_s = 120˚ (northern hemisphere summer), but we also ran selected simulations at L_s = 300˚ (northern hemisphere winter) for a seasonal comparison. Each run began before the surface energy balance became positive (*i.e.*, more energy being imparted to the surface than leaving it) and lasted until it became negative once more. In the VL1 runs the local mean solar time (LMST) ranged from 4.63h – 18.63h. In the Phoenix runs the LMST ranged from 3.45h – 21.45h, encompassing the hours during which polar summer experiences the most direct insolation.

The LES were run under idealized conditions in order to clearly distinguish the influences of insolation and elevation from more localized and situation-dependent conditions. For example, the LES setup did not include topography or variations in atmospheric dust content. In addition, H_2O vapor/ice, and CO_2 ice were not accounted for in the simulations. The LES used periodic boundary conditions to effectively simulate the atmosphere over a vast plain.

One simulation was run with a grid spacing of 50 m to determine if finer resolution of the turbulent structures had an effect on wind distributions. To capture a broad range of turbulent structures within realistic computational constraints, we chose the VL1 wintertime case in the late morning, when structures are small but well-developed. This simulation used an additional 200×200×99 nested grid with a horizontal grid interval of 50 m. The LES was run with the same stretched vertical grid spacing as the coarser grid, and a dynamical timestep of 0.5 s. This simulation was started using a prior 100 m restart file, and was run for more than an hour (ending at 11.63 h LMST).

Typically, LES initial conditions are specified from vertical soundings from lower resolution mesoscale simulations. Initial temperature and pressure profiles for the LES were specified in this way. However, realistic wind profiles can be complex and change during the day, so in order to isolate the effects on the boundary layer convection due to differing wind profiles, we used three idealized wind profiles chosen for their relative simplicity. Other than the initial wind profile, no wind forcing occurred for the duration of the simulations. The three initial wind profiles were defined as follows (see Figure 3):

1) Case 1, no wind: $u(z, t=0) = 0, v(t=0) = 0$

2) Case 2, uniform wind: $u(z, t=0) = 5\ \mathrm{m\ s^{-1}}, v(t=0) = 0$

3) Case 3, wind speed shear:
$u(z, t=0) \approx 1.46z + 2, v(t=0) = 0$,
such that $u(z=0, t=0) \approx 2\ \mathrm{m\ s^{-1}}$,
and $u(z=12\ \mathrm{km}, t=0) \approx 20\ \mathrm{m\ s^{-1}}$

To test the effects of wind with superimposed speed shear, we also ran two modified versions of Case 3, in which the initial near surface wind speed $u(z=0, t=0)$ was set to 10 m s^{-1} and 20 m s^{-1} (which quickly decelerated to create a logarithmic profile near the surface), so that $u(z, t=0) \approx 1.46z + 10$ and $u(z, t=0) \approx 1.46z + 20$, respectively. We call the initial conditions "intermediate winds with wind shear" and "strong winds with wind shear", respectively. We chose to run these LES at the Phoenix landing site to approximate the effects of the polar vortex, which should strongly influence the near-surface wind regime at high latitudes.

Results

In order to determine how the developing convective boundary layer influences the potential for sand saltation and

saltation-induced dust lifting, we have plotted the probability distribution of friction velocity (u_*) modeled by the LES at the two different landing sites. For reference, using the empirically derived equations from (Greeley and Iversen 1985), we estimate approximate fluid threshold friction velocities u_{*t} for 100 µm basalt sand to be as follows in Table 3. These values were calculated at local noon (LMST) when air density is at a minimum; therefore, they represent the maximum daily fluid saltation threshold.

Table 3. Friction velocity thresholds (table3.txt).

Location	Season (L_s)	u_{*t}
VL1	120º	1.8 m s^{-1}
Phoenix	120º	1.7 m s^{-1}
VL1	300º	1.6 m s^{-1}

Case 1

In the simplest of LES, there is no mean wind, so that all wind gusts (measured here at the surface as high values of friction velocity) are produced solely by the development of buoyantly-induced turbulence within the convective boundary layer. One measure of insolation-driven buoyancy is the vertical potential temperature gradient at the surface ($\partial\theta_s/\partial z$, the surface static (in)stability): values less than zero indicate static instability, for which solar forcing has heated the surface more than the near-surface atmosphere, triggering dry convective turbulence that tries to mix heat between the two.

Figure 4 shows the distribution of surface static instability and friction velocity at ten local times (8.63h – 17.63h LMST) across the VL1 domain. The surface air is statically unstable by midmorning, reaches a maximum of static instability (~ -20 K/m) around local noon, and gradually grows less statically unstable as the afternoon progresses. Measurements from Mars Pathfinder also indicated a high degree of instability during the daytime (Schofield et al., 1997). By late afternoon (17.63h LMST), the sun is low in the sky and can no longer heat the surface enough to produce a negative vertical potential temperature gradient; at this point the convective boundary layer begins to collapse. Friction velocity distributions broaden throughout the morning and early afternoon, reflecting increased gustiness produced by buoyantly-driven turbulence within the boundary layer. The peak gustiness, shown in the u_* distributions, occurs in the early afternoon (12.63h – 14.63h LMST), shortly after the surface static instability has peaked and the boundary layer has had time to react to this strong gradient with vigorous circulations. According to Mars lander observations, dust devil activity peaks in the early afternoon, consistent with our LES results (e.g., Ellehoj et al. 2010, Greeley et al. 2006). Although it is difficult to see in Figure 4, a few grid points in the LES domain do experience friction velocities that surpass the estimated saltation threshold of 1.8 m s^{-1} during the hours of peak gustiness, demonstrating that convective turbulence alone, with no imposed mean wind, has the potential to produce particle entrainment on Mars.

Figure 5 shows similar plots of surface static stability and friction velocity at the Phoenix site, using the same axis ranges and similar local times as in Figure 4. As at the VL1 site, instability at the Phoenix site reaches a maximum around local noon, although at such northern latitudes insolation is not direct enough to produce as strong a vertical potential temperature gradient, reaching to only ~ -16 K/m (at L_s = 120º the VL1 site the sun peaks at ~89.4˚ above the horizon; at the Phoenix site it peaks at ~43.4˚ above the horizon). As the insolation decreases during the afternoon, the static instability decreases but much more slowly than at the VL1 site, since during the polar summer the sun is above the horizon at all times and approaches the horizon at a shallower angle. Thus the convective boundary layer at the Phoenix site may not produce such vigorous turbulence as that at the VL1 site, but buoyantly-driven turbulence takes longer to subside in the evening. This result is reflected in the distribution of friction velocities in Figure 5, which never reach the same maxima as those at the VL1 site (and thus are less likely to mobilize sand) but which take longer to weaken in the afternoon.

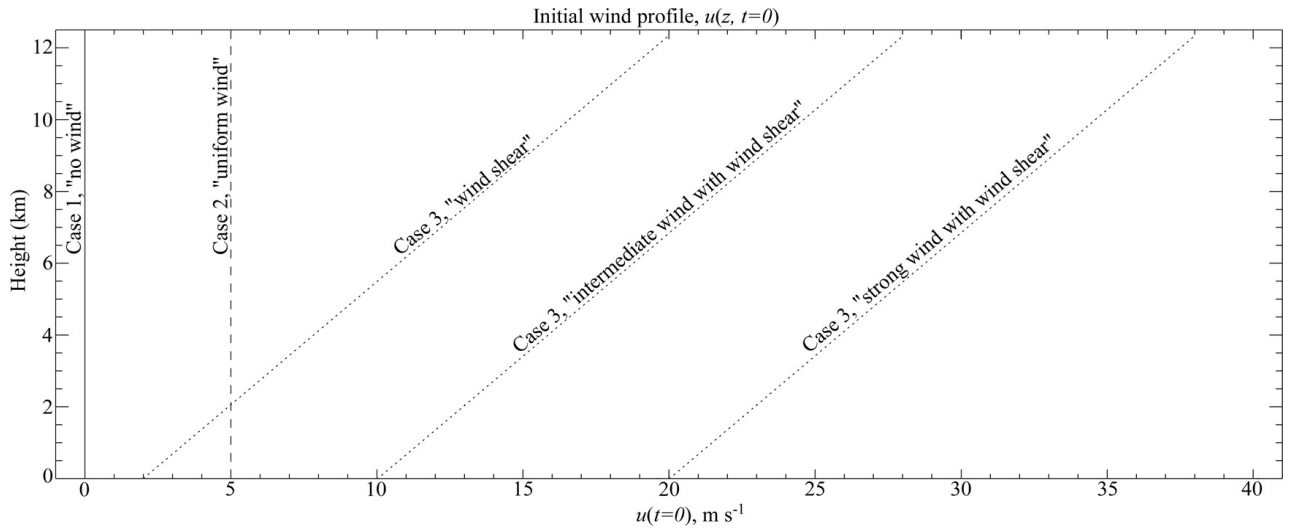

Figure 3. Initial wind velocity profiles used in the LES (figure3.jpg) (figure3.txt).

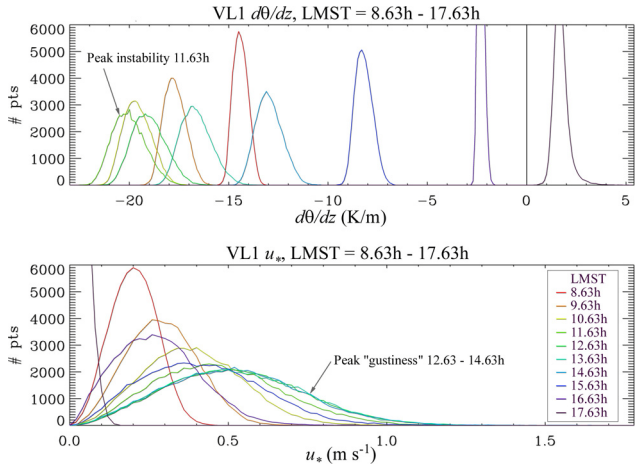

Figure 4. Viking Lander 1 site LES domain distributions of surface static stability (top) and friction velocity (bottom) from morning to late afternoon (figure4.jpg) (figure4.txt).

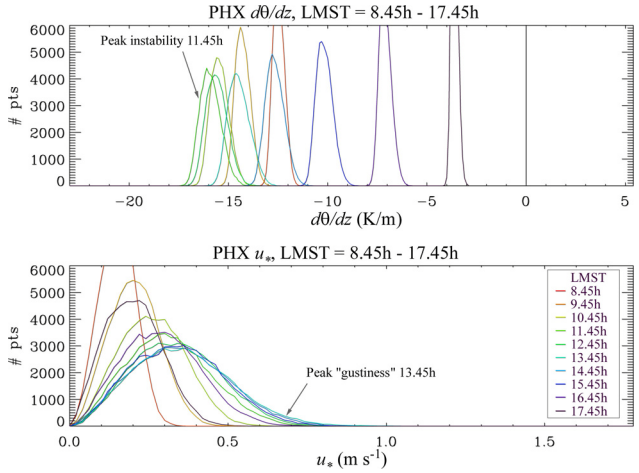

Figure 5. Phoenix landing site LES domain distributions of surface static stability (top) and friction velocity (bottom) from morning to late afternoon (figure5.jpg) (figure5.txt).

Cases 2 and 3

The idealized initial wind profiles (see Figure 3) proved to have a significant impact on the distribution of friction velocity, particularly in the high tail of the distribution. Figure 6 shows resulting friction velocities from the three different wind profile cases at four local times (the solid lines denoting Case 1 output are also shown in Figure 4 and follow the same color scheme). At midmorning (8.63h LMST), the u_* distributions best reflect the influence of initial near-surface wind speeds (0 m/s for Case 1, 5 m/s for Case 2, and 2 m/s for Case 3). By late morning to early afternoon, the distributions have widened and nearly overlap one another, although the uniform wind and wind shear cases do exhibit slightly stronger wind gusts than the no wind case. In all cases, noontime broadening of the friction velocity distribution indicates that buoyantly-driven turbulence dominates over any wind-shear-driven turbulence caused by the initial wind structure (as evidenced by broad convective cells such as those in Figure 1). In the late afternoon (16.63h LMST), convective turbulence has weakened and the friction velocity distributions in the no wind and uniform wind cases are beginning to revert back to their initial distribution. The wind shear case, however, is still experiencing downward mixing of stronger winds (i.e., higher momentum) from aloft, and thus its friction velocities are still stronger than those of the other wind profile cases.

The Phoenix site LES show a fairly similar pattern (see Figure 7), with a few slight differences. As discussed above, convective activity at such high latitudes is not strong enough to widen friction velocity distributions as much as at the VL1 site, and this is reflected in all three initial wind profile cases. A secondary effect of this weaker activity is that it allows the initial wind structure at the Phoenix site to more prominently influence the turbulence – the difference between the no wind case and the other wind cases is larger in the late morning (11.45h LMST) than at the VL1 site. As expected, the effects of insolation on producing vigorous convective turbulence (and therefore wind gustiness) are dependent on latitude as well as the initial wind structure. In reality, background winds will likely change continuously throughout the day (e.g., as tidally- or topographically-driven winds shift and interact), so that the wind structure of the previous hours should be considered when superimposing LES friction velocity distributions on mesoscale winds.

Case 2 at L_s = 300º

Figure 8 shows a comparison of friction velocity distributions at L_s = 120º and 300º. At 8.63h during winter, the sun is still relatively low in the sky and has not yet produced enough convective activity to widen the wind distribution. By noon, both simulations show that convective turbulence is well developed, although it is weaker in the winter (see the value of friction velocity at the distribution peaks). Late in the day, the solar incidence angle is similar in both simulations (a result of Mars' eccentric orbit), and this is reflected in the overlapping wind distributions. Not surprisingly, wintertime convective activity is less likely to produce wind gusts strong enough to saltate grains on Mars.

Case 3 with superimposed uniform wind

We tested the effects of initial wind speed shear with a superimposed uniform wind at the Phoenix landing site with surface winds of 2, 10, and 20 m s^{-1}. Figure 9 shows u_* distributions for each of these cases (the solid lines show the same distributions plotted as dotted lines in Figure 7). Not surprisingly, the stronger wind distributions correspond to those beginning with stronger initial wind speeds.

Figure 10 shows the effect of an increasing background wind on convective cells. In the first column, the Case 3 convection cells appear largely undistorted. Because of the initial wind velocities, winds on the downwind edges of convection cells (on the right side) have higher friction velocities as the background wind is constructively superimposed on the convective wind pattern; likewise, winds on the upwind edges of convection cells are lower as the background wind is destructively superimposed on the convective wind pattern. In the center and right columns, increasing initial wind

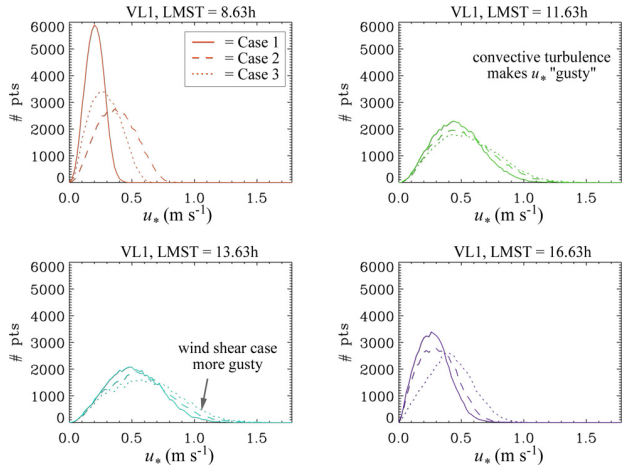

Figure 6. Histograms of friction velocities from the Viking Lander 1 site at L_s = 120º (figure6.jpg) (figure6.txt).

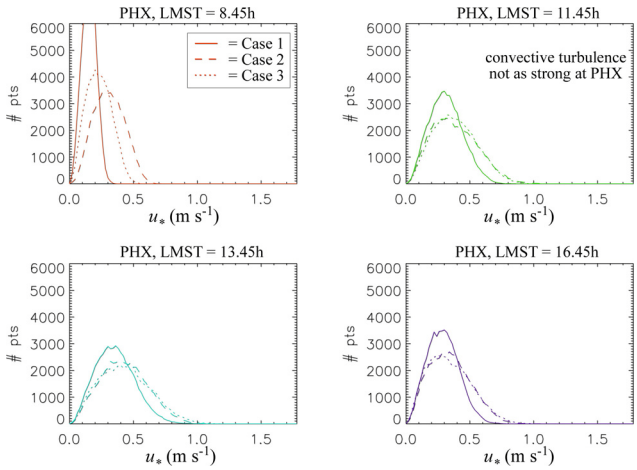

Figure 7. Histograms of friction velocities from the Phoenix lander site at L_s = 120º (figure7.jpg) (figure7.txt)

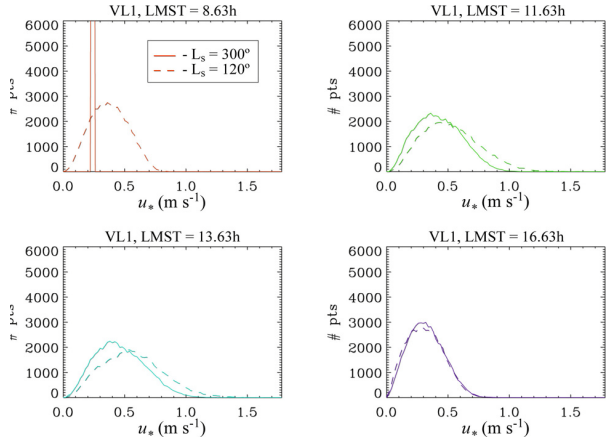

Figure 8. Histograms of friction velocities from the Viking Lander 1 site at Ls = 120º (summer) and 300º (winter) (figure8.jpg) (figure8.txt).

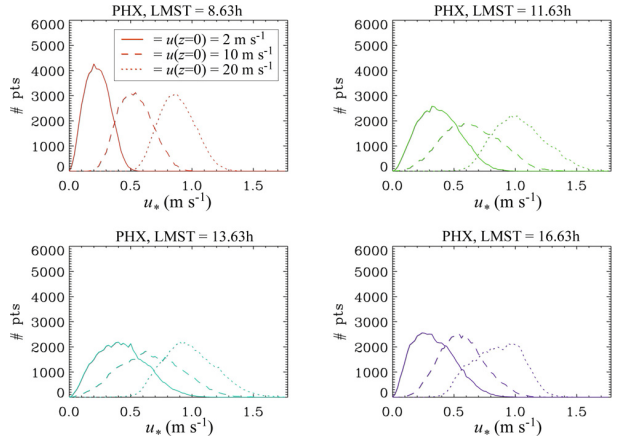

Figure 9. Histograms of friction velocities from the Phoenix lander site showing initial wind cases of weak, intermediate, and strong winds with wind shear (figure9.jpg) (figure9.txt).

velocities "blur" the edges of convective structures and destroy the smaller features. The blurring occurs as the mechanical turbulence from the initial wind interacts with the buoyantly-driven turbulence that produces the cells. Although even at a surface wind of 20 m s^{-1}, the convection cells are still well defined, it is likely that at even higher wind speeds and wind shear, the convective structures will be fully overwhelmed, replaced by horizontal rolls that are transverse to the background wind.

In Figure 9, note that as the day progresses the wind distributions take on shapes that do not conform to a Weibull distribution (compare with Figure 2). It is likely that as background wind patterns become more complex and interfere with the convective structures, friction velocity distributions will deviate more from the classic Weibull shape.

Discussion: Effect of local conditions on Weibull fit parameters

The goal of this work is to devise a simple way to represent subgrid-scale wind gusts in lower resolution atmospheric models. Thus we provide a discussion of fits of our LES output to the two parameter Weibull PDF.

Figure 11 shows Weibull fit shape (k) and scale (c) parameters for each of the three initial wind profiles as a function of local time at the Viking Lander 1 site. Supplementary Figure 1 shows fits to the Case 1 LES, showing that the fit to a Weibull is adequate for most output timesteps in this simulation. Regardless of the initial wind conditions, the shape parameter ranges from 2.5-3 during the peak gusty hours, values significantly larger than those previously used by others to account for wind variance (see discussion in the Background section). Scale parameters range from 0.2-0.6 m s^{-1}, 0.4-0.65 m s^{-1}, and 0.3-0.7 m s^{-1} for initial wind Cases 1, 2, and 3, respectively. Higher values estimated for more complex initial winds reflect the additional energy they input to the LES domain, producing gustier winds. The highest scale parameter value occurs late in the day of the Case 3 LES, when convective turbulence is well developed and high winds aloft have had a chance to mix downward towards the surface. By using the method of maximum likelihood, the fits have been designed to consider the mode of the wind distribution rather than the high tail (in

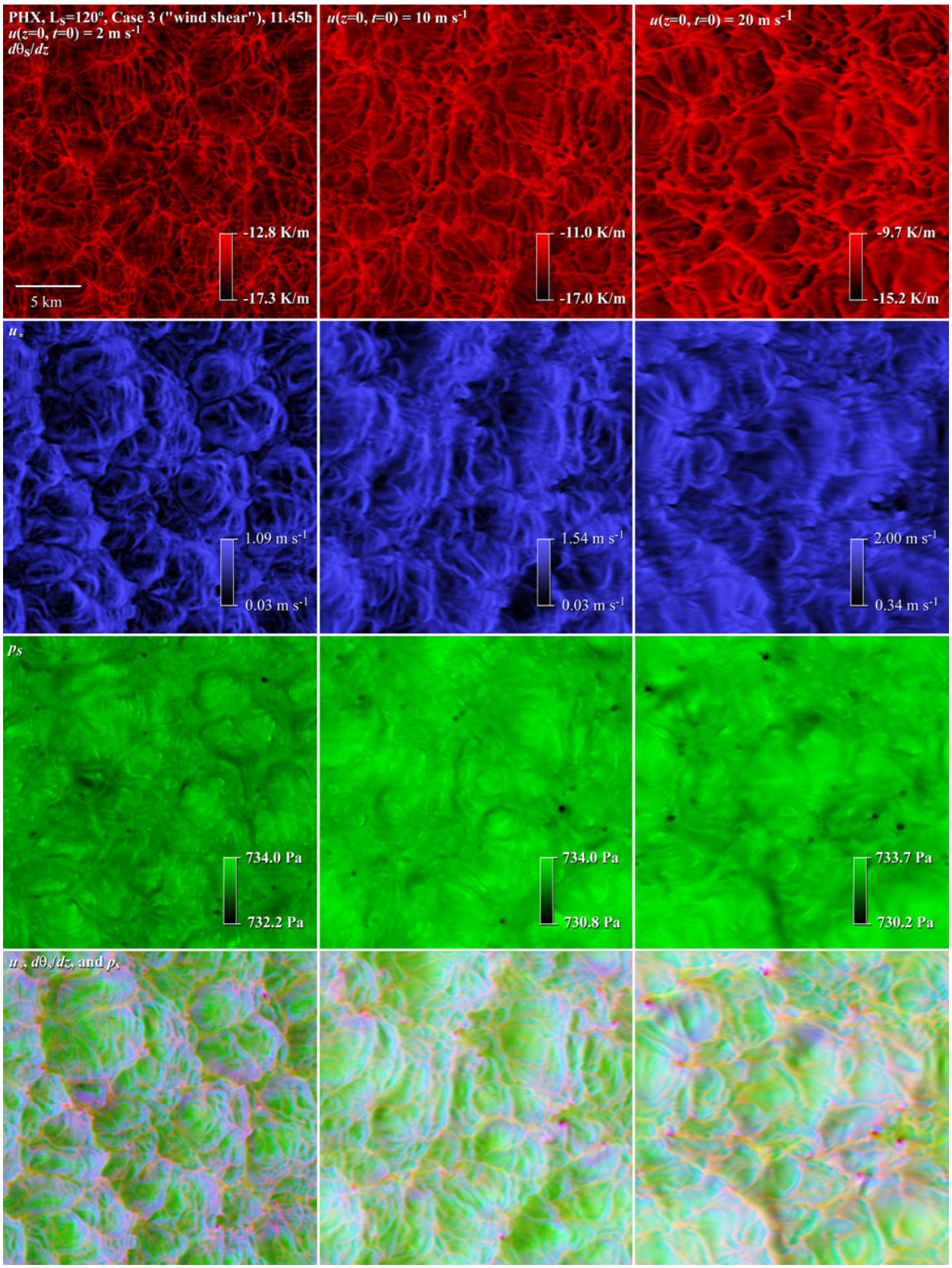

Figure 10. Horizontal near-surface slices through the Phoenix landing site LES with Case 3 initial winds. Top row: static stability $\partial\theta_s/\partial z$; second row: friction velocity u_*, third row: air pressure p_s; bottom row: composite of the first three rows (figure10.jpg).

which we are most interested). As a result, the two parameter values may not produce the best possible Weibull fit to the high tail. This is a known issue that we plan to address in future work.

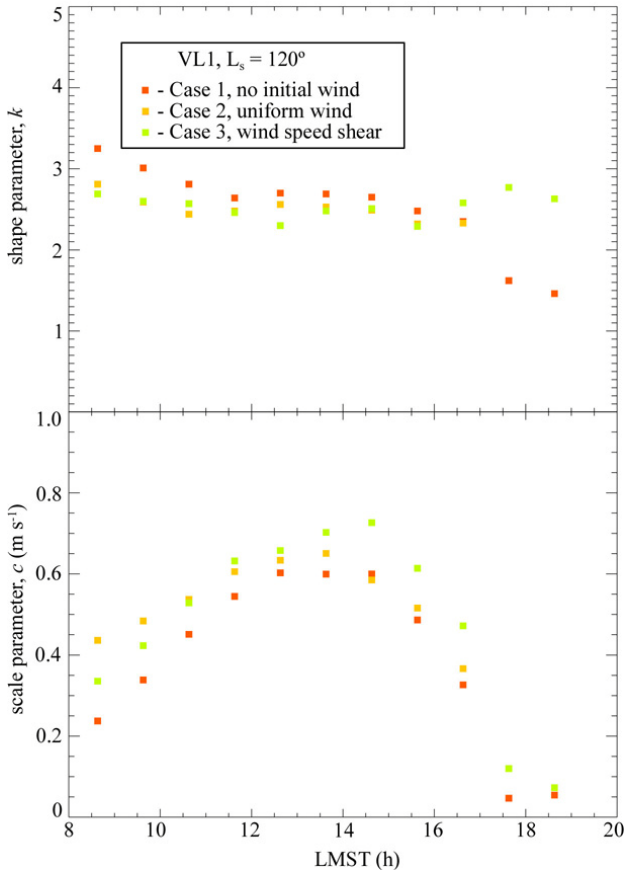

Figure 11. Shape parameter *k* and scale parameter *c* values at the Viking Lander 1 site for initial wind Cases 1, 2, and 3 (figure11.jpg) (figure11.txt).

Figure 12 shows Weibull fit parameters for the three initial wind profiles as a function of local time at the Phoenix lander site. Like at the Viking Lander 1 site, shape parameters range from 2.5-3 during peak insolation hours. Scale parameters range from 0.2-0.4 m s^{-1}, 0.35-0.5 m s^{-1}, and 0.25-0.5 m s^{-1} for initial wind Cases 1, 2, and 3, respectively. Again, the Case 1 "no wind" initial condition leads to lower scale parameter estimates. Scale parameter values are lower than those at the Viking Lander 1 site, reflecting the less vigorous convection at higher latitudes caused by less direct sunlight.

Figure 13 compares the scale and shape parameters from the summer and winter LES at the Viking Lander 1 site. As with previous simulations, shape parameters range from 2.5-3 at both times of the year. In the winter, the scale parameter ranges from 0.25-0.5 m s^{-1} during the day; in the summer the scale parameter varies from 0.4-0.65 m s^{-1} during the day. The lower wintertime scale parameter values reflect less vigorous buoyantly-driven convection caused by less direct sunlight at this season. As a result, the high wind speed tail in the winter will be shorter than it is during the summer.

The single outlined point in green corresponds to the

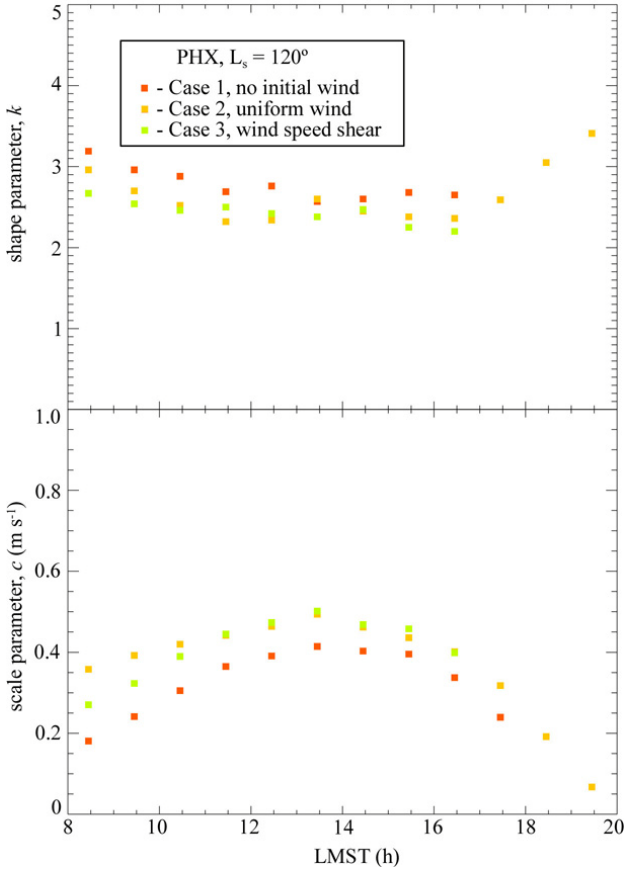

Figure 12. Shape parameter *k* and scale parameter *c* values at the Phoenix lander site for initial wind Cases 1, 2, and 3 (figure12.jpg) (figure12.txt).

wintertime simulation made with a grid spacing of 50 m (see Table 1). The shape and scale parameter estimates are similar to those made for this local time in the larger, lower resolution domain in blue. This implies that higher resolution simulations, at least down to a grid spacing of 50 m, do not significantly change the results of our simulations with a grid spacing of 100 m.

Differences in Weibull fit parameters are seen in the LES using the Case 3 initial wind profiles, especially those with a superimposed uniform wind. Figure 14 shows these parameters. The fits to these wind distributions (see Supplemental Figure 2) are significantly worse than those for the VL1 Case 1 simulation (see Supplemental Figure 1), likely as a result of the complex background wind regime in which strong winds compete with convective turbulence for dominance over the LES domain (see Figure 9). Fits to the Weibull PDF appear to be most robust in simple wind regimes with no strong background winds. Despite the poor fits of the Phoenix lander Case 3 simulation output, we consider our fit parameters to be an improvement over previous work. However, it is clear that a better fit method would further improve characterization of the wind distribution, and the statistical significance of the Weibull PDF remains to be further explored.

In Figure 14, the shape parameter varies from 2.5-3, 3-4, and

4-7 for Case 3 winds with a uniform background wind of 2 m s^{-1}, 10 m s^{-1}, and 20 m s^{-1}, respectively (see Table 1 and Figure 3). With an increasingly strong initial wind, the shape parameters signify narrower wind distributions. The scale parameters vary from 0.25-0.5 m s^{-1}, 0.6-0.7 m s^{-1}, and 0.9-1.15 m s^{-1}, respectively, during hours of peak insolation. It is these values that lead to the stronger high wind speed tail for these simulations, visible in Figure 9.

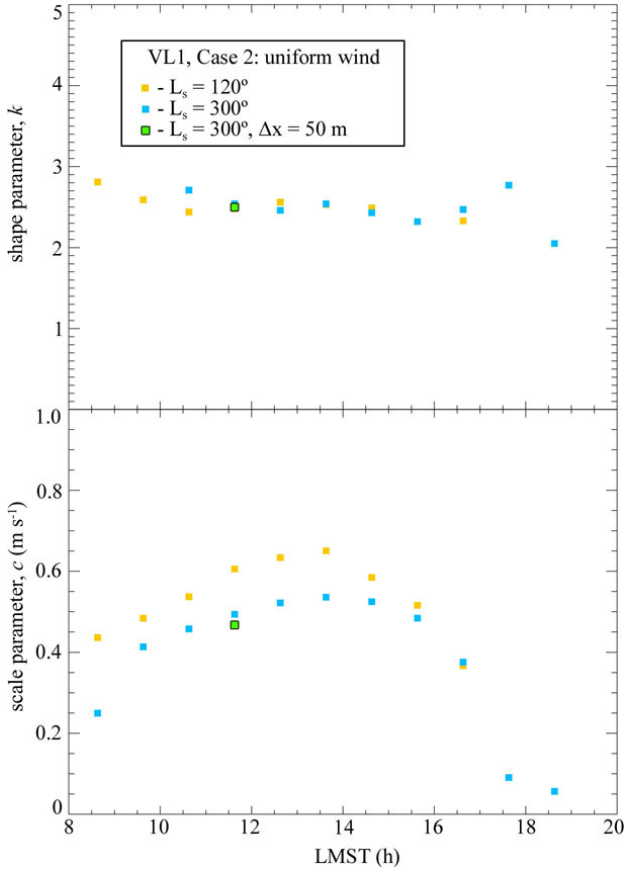

Figure 13. Shape parameter k and scale parameter c values at the Viking Lander 1 site for initial wind Cases 2 at L_s = 120° and 300°. Values from L_s = 120° are the same shown in Figure 12. The outlined point indicates fit parameters for the single output timestep from the domain with 50 m grid spacing. (figure13.jpg) (figure13.txt).

The scale parameter c varies with location (Figures 11 and 12), season (Figure 13) and background wind (Figure 14), which in theory makes a universal parameterization difficult to define. This parameter has been assumed to approximately equal the local friction velocity in low resolution models as a way to account for the diurnal increase in wind gusts (Newman et al. 2002; Basu et al. 2004). Our results indicate that this is indeed a fair approximation, at least for the conditions we have simulated thus far (see Figure 15). We recommend that, until better estimates and methods are available, those trying to account for the broadening of the wind distribution during the day with the Weibull PDF use a shape parameter between 2.5-3 and a scale parameter approximately equal to the local friction velocity. These values may not hold under all conditions, such as under strong

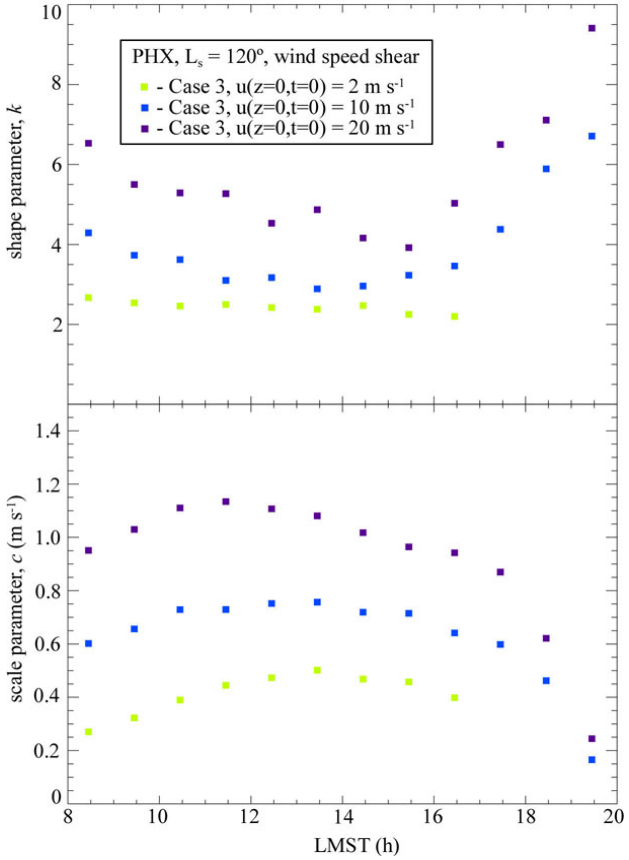

Figure 14. Shape parameter k and scale parameter c values at the Phoenix lander site for initial wind Case 3 with a weak, intermediate, and strong superimposed uniform wind (note that the vertical scales have changed relative to Figures 11-13) (figure14.jpg) (figure14.txt).

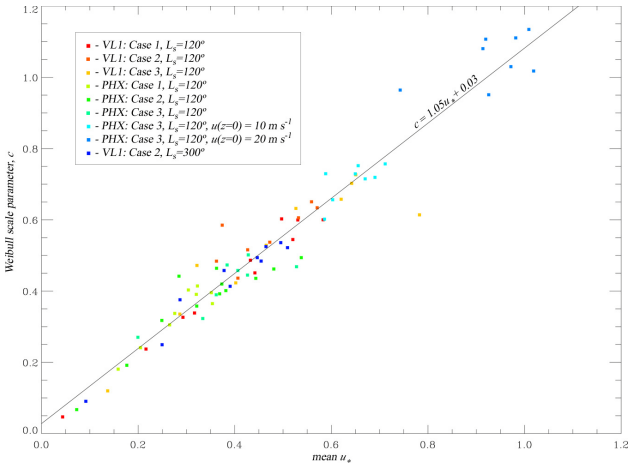

Figure 15. Scale parameter c versus friction velocity u_* for all 100 m grid LES, showing that the scale parameter is similar to u_* values in our simulations (figure15.jpg) (figure15.txt).

winds with wind shear (see Figure 14) or over icy surfaces, so we caution that these values not be considered either absolute or final. Further exploration of the parameter space is required to fully understand how wind distributions are affected by the

many different, and often extreme, atmospheric and surface conditions that occur on Mars.

Conclusions

Large-eddy simulations, using idealized initial wind profiles at two lander locations, have demonstrated that daytime convective turbulence can significantly increase the likelihood of particle entrainment on Mars, and that the degree of this enhancement is dependent on (at least) several factors. Wind gustiness (i.e., strong, intermittent friction velocities) generally increases with insolation, such that the strongest winds produced by convective turbulence would occur when the sun is highest in the sky, as dictated by local time, latitude, and season. This occurs even when there is no initial mean wind, such that convective turbulence alone may produce occasional wind gusts that exceed the saltation threshold.

The distribution of friction velocities is also dependent on the initial wind profile, which influences wind gustiness throughout the day and has a variable impact depending on insolation and local time. Such imposed "mean wind" structures elevate peak friction velocities, increasing the likelihood that particle entrainment will occur, even several hours later in the day. When the sun is high in the sky, convective activity reaches its peak and, if vigorous enough, can nearly override the initial wind structure. Later in the day when convective activity subsides, the initial wind structure once again dominates the distribution of friction velocities. In the case where initial winds included shear such that stronger winds blew aloft (which is likely typical of most wind profiles on Mars), convective turbulence throughout the day continued to mix down momentum from these stronger winds, leading to enhanced peak friction velocities that persist into later afternoon hours than would otherwise occur.

Strong initial winds, such as those combining a uniform wind and shear such that wind speed increases with altitude, strongly impact the distribution of friction velocities. Such strong winds interfere with the convective structure, smearing the updraft regions and destroying smaller convective cells. These winds produce friction velocity distributions that are complex and difficult to fit to a Weibull probability density function, indicating that more realistic conditions typical of Mars can easily produce wind distributions that are difficult to analytically quantify.

Despite the imperfect fit quality, some analytical method of summarizing convectively-driven wind distributions is desirable to account for these subgrid-scale motions in lower resolution atmospheric models, such as mesoscale models. We find that, until a better method of estimating such parameters is available, Weibull fit parameters may be applied using the general methodologies of either Newman et al. (2002), Basu et al. (2004), or Michaels (2006) (and Michaels and Rafkin (2008)), employing values of 2.5-3 for the shape parameter and a value equal to the lower resolution model's estimation of u_* for the scale parameter. We caution that these values are likely to be inaccurate in some conditions, such as high wind energy environments, which appear to require shape parameters two to three times the above range of values. We will continue to explore the overall parameter space to determine the best way(s) to account for subgrid-scale turbulent broadening of the friction velocity distribution that greatly enhances the atmosphere's potential aeolian effectiveness during the daytime on Mars. Continuous near-surface high frequency wind measurements are necessary to validate these results.

Directory of supporting data

root directory

- fenton_mars_2010_0007.pdf this file
- Figure 1 figure1.jpg full-resolution image
- Figure 2 figure2.jpg full-resolution image
- Figure 3 figure3.jpg full-resolution image; figure3.txt source data in tabular format
- Figure 4 figure4.jpg full-resolution image; figure4.txt source data in tabular format
- Figure 5 figure5.jpg full-resolution image; figure5.txt source data in tabular format
- Figure 6 figure6.jpg full-resolution image; figure6.txt source data in tabular format
- Figure 7 figure7.jpg full-resolution image; figure7.txt source data in tabular format
- Figure 8 figure8.jpg full-resolution image; figure8.txt source data in tabular format
- Figure 9 figure9.jpg full-resolution image; figure9.txt source data in tabular format
- Figure 10 figure10.jpg full-resolution image
- Figure 11 figure11.jpg full-resolution image; figure11.txt source data in tabular format
- Figure 12 figure12.jpg full-resolution image; figure12.txt source data in tabular format
- Figure 13 figure13.jpg full-resolution image; figure13.txt source data in tabular format
- Figure 14 figure14.jpg full-resolution image; figure14.txt source data in tabular format
- Figure 15 figure15.jpg full-resolution image; figure15.txt

- Supplemental Figure 1 suppfigure1.jpg full-resolution image; suppfigure1.txt source data in tabular format
- Supplemental Figure 2 suppfigure2.jpg full-resolution image; suppfigure2.txt source data in tabular format

- Table 1 table1.txt source data
- Table 2 table2.txt source data
- Table 3 table3.txt source data

Acknowledgements

This research was supported by a NASA Mars Fundamental Research Program grant (NNX08AU36G).

References

Armstrong, J. C. and C. B. Leovy (2005) "Long term wind erosion on Mars" Icarus 176, 57-74. doi:10.1016/j.icarus.2005.01.005

Basu, S., M. I. Richardson and R. J. Wilson (2004) "Simulation of the Martian dust cycle with the GFDL Mars GCM" Journal of Geophysical Research 109, E11006. doi:10.1029/2004JE002243

Cantor, B. A., K. M. Kanak and K. S. Edgett (2006) "Mars Orbiter Camera observations of Martian dust devils and their tracks (September 1997 to January 2006) and evaluation of theoretical vortex models" Journal of Geophysical Research 111, E12002. doi:10.1029/2006JE002700

Deardorff, J. W. (1980) "Stratocumulus-capped mixed layers derived from a three-dimensional model" Boundary-Layer Meteorology 18, 495-527. doi:10.1007/BF00119502

Ellehoj, M. D. et al. (2010) "Convective vortices and dust devils at the Phoenix Mars mission landing site" Journal of Geophysical Research 115, E00E16. doi:10.1029/2009JE003413.

Haberle, R. M., J. R. Murphy and J. Schaeffer (2003) "Orbital change experiments with a Mars general circulation model" Icarus 161, 66-89. doi:10.1016/S0019-1035(02)00017-9

Greeley, R. and J. D. Iversen (1985) Wind as a geological process, Cambridge University Press, Cambridge.

Greeley, R. et al. (2006) "Active dust devils in Gusev crater, Mars: Observations from the Mars Exploration Rover Spirit" Journal of Geophysical Research 111, E12S09. doi:10.1029/2006JE002743

He, Y., A. H. Monahan, C. G. Jones, A. Dai, S. Biner, D. Caya and K. Winger (2010) "Probability distributions of land surface wind speeds over North America" Journal of Geophysical Research, 115, D04103. doi:10.1029/2008JD010708

Holstein-Rathlou, C. et al. (2010) "Winds at the Phoenix landing stie" Journal of Geophysical Research, 115, E00E18. doi:10.1029/2009JE03411

Iversen, J. D. and B. R. White (1982) "Saltation threshold on Earth, Mars and Venus" Sedimentology 29, 111-119. doi: 10.1111/j.1365-3091.1982.tb01713.x

Kahre, M. A., J. R. Murphy and R. M. Haberle (2006) "Modeling the Martian dust cycle and surface dust reservoirs with the NASA Ames general circulation model" Journal of Geophysical Research 111, E06008. doi:10.1029/2005JE002588

Lorenz, R. D. (1996) "Martian surface wind speeds described by the Weibull distribution" Journal of Spacecraft and Rockets 33, 754-756. doi: 10.2514/3.26833

Michaels, T. I. (2002) M.S. Thesis, San Jose State University, San Jose.

Michaels, T. I. and S. C. R. Rafkin (2004) "Large-eddy simulation of atmospheric convection on Mars" Quarterly Journal of the Royal Meteorological Society 130, 1251-1274. doi:10.1256/qj.02.169

Michaels, T. I. (2006) "Numerical modeling of Mars dust devils: Albedo track generation" Geophysical Research Letters 33, L19S08. doi:10.1029/2006GL026268

Michaels, T. I. (2008) "Meteorological predictions for candidate 2007 Phoenix Mars Lander sites using the Mars Regional Atmospheric Modeling System (MRAMS)" Journal of Geophysics Research 113, E00A07. doi:10.1029/2007JE003013

Newman, C. E., S. R. Lewis, P. L. Read and F. Forget (2002) "Modeling the Martian dust cycle, 1. Representations of dust transport processes" Journal of Geophysical Research 107, 5123. doi:10.1029/2002JE001910

Rafkin, S. C. R., R. M. Haberle and T. I. Michaels (2001) "The Mars regional atmospheric modeling system: Model description and selected simulations" Icarus 151, 228-256. doi:10.1006/icar.2001.6605

Rafkin, S. C. R. and T. I. Michaels (2003) "Meteorological predictions for the 2003 Mars Exploration Rover high-priority landing sites" Journal of Geophysical Research 108, 8091. doi:10.1029/2002JE002027

Schofield, J. T., J. R. Barnes, D. Crisp, R. M. Haberle, S. Larsen, J. A. Magalhães, J. R. Murphy, A. Seiff and G. Wilson (1997) "The Mars Pathfinder Atmospheric Structure Investigation/Meteorology (ASI/MET) Experiment" Science 278, 1752-1757. doi:10.1126/science.278.5344.1752

Spiga, A. and F. Forget (2009) "A new model to simulate the Martian mesoscale and microscale atmospheric circulation: Validation and first results" Journal of Geophysical Research 114, E02009. doi:10.1029/2008JE003242

Spiga, A., F. Forget, S. R. Lewis and D. P. Hinson (2010) "Structure and dynamics of the convective boundary layer on Mars as inferred from large-eddy simulations and remote-sensing measurements" Quarterly Journal of the Royal Meteorological Society 136, 414-428. doi:10.1002/qj.563

Sullivan, R. et al. (2008) "Wind-driven particle mobility on Mars: Insights from Mars Exploration Rover observations at "El Dorado" and surroundings at Gusev Crater" Journal of Geophysical Research 113, E06S07. doi:10.1029/2008JE003101

Toigo, A. D., M. I. Richardson, R. J. Wilson, H. Wang and A. P. Ingersoll (2002) "A first look at dust lifting and dust storms near the south pole of Mars with a mesoscale model" Journal of Geophysical Research 107, 5050. doi:10.1029/2001JE001592

Toigo, A. D., M. I. Richardson, S. P. Ewald and P. J. Gierasch (2003) "Numerical simulation of Martian dust devils" Journal of Geophysical Research 108, 5047. doi:10.1029/2002JE002002

Tuller, S. E. and A. C. Brett (1984) "The Characteristics of wind velocity that favor the fitting of a Weibull Distribution in wind speed analysis" Journal of Applied Meteorology 23, 124-134. doi:10.1175/1520-0450(1984)023<0124:TCOWVT>2.0.CO;2

Tyler, D. (2008) "Mesoscale and large-eddy simulation model studies of the Martian atmosphere in support of Phoenix" Journal of Geophysical Research 113, E00A12. doi:10.1029/2007JE003012